Analysis of gas jetting and fumarole acoustics at Aso Volcano, Japan

Kathleen **McKee** (kfmckee@alaska.edu)*[a], David **Fee** (dfee1@alaska.edu)[a], Akihiko **Yokoo** (yokoo.akihiko.5a@kyoto-u.ac.jp)[b], Robin S. **Matoza** (matoza@geol.ucsb.edu)[c], Keehoon **Kim** (kim84@llnl.gov)[d]

[a]*Geophysical Institute, Alaska Volcano Observatory, Wilson Alaska Technical Center, University of Alaska Fairbanks, 903 Koyukuk Drive – P.O. Box 757320, Fairbanks, Alaska 99775*

[b]*Aso Volcanological Laboratory, Institute for Geothermal Sciences, Graduate School of Science, Kyoto University, 5280 Kawayo, Minami-Aso, Kumamoto 869-1404, Japan*

[c]*Department of Earth Science and Earth Research Institute, Webb Hall MC 9630, University of California, Santa Barbara, California, 93106*

[d]*Lawrence-Livermore National Laboratory, 7000 East Avenue, Livermore, California 94550*

**Corresponding author*

Abstract

The gas-thrust region of a large volcanic eruption column is predominately a momentum-driven, fluid flow process that perturbs the atmosphere and produces sound akin to noise from jet and rocket engines, termed "jet noise". We aim to enhance understanding of large-scale volcanic jets by studying an accessible, less hazardous fumarolic jet. We characterize the acoustic signature of ~2.5 meter wide vigorously jetting fumarole at Aso Volcano, Japan using a 5-element infrasound array located on the nearby crater. The fumarole opened on 13 July 2015 on the southwest flank of the partially collapsed pyroclastic cone within Aso Volcano's Naka-dake crater and had persistent gas jetting, which produced significant audible jet noise. The array was ~220 meters from the fumarole and 57.6 degrees from the vertical jet axis, a recording angle not typically feasible in volcanic environments. Array processing is performed to distinguish fumarolic jet noise from wind. Highly correlated periods are characterized by sustained, low-amplitude signal with a 7-10 Hz spectral peak. Finite difference time domain method numerical modeling suggests the influence of topography near the vent and along the propagation path significantly affects the spectral content, complicating comparisons with laboratory jet noise. The fumarolic jet has a low estimated Mach number (0.3 to 0.4) and measured temperature of ~260°C. The Strouhal number for infrasound from volcanic jet flows and geysers is not known; thus we assume a peak Strouhal number of 0.19 based on pure-air laboratory experiments. This assumption leads to an estimated exit velocity of the fumarole of ~79 to 132 m/s. Using published gas composition data from 2003-2009, the fumarolic vent area estimated from thermal infrared images, and estimated jet velocity, we estimate total volatile flux at ~160 - 260 kg/s (14,000 – 23,000 t/d).

1. Introduction

The sound produced by jet flow from human-made jet engines and rockets is called jet noise. Research on jet noise shows that its signal characteristics depend upon the jet's velocity,

temperature, and nozzle diameter (Woulff and McGetchin, 1976; Tam, 1995; Tam, 1998). Human-made jets and their noise spectra exhibit self-similarity, with the spectral shape remaining relatively constant and scaling according to the frequency, diameter, and velocity (Tam et al., 1996). Volcanoes generate jet flows at a variety of scales, from low-level gas jetting to violent subplinian-plinian volcanic jets. Recent investigations into infrasonic signals associated with volcanic jet flows have suggested that the self-similarity of jet noise may extend even to large (meters to hundreds of meters) volcanic length scales (Matoza et al., 2009; Fee et al., 2013; Matoza et al., 2013). Thus, similar relationships are hypothesized to exist between volcanic jet noise and volcanic jet flow parameters (e.g. vent diameter and jet velocity and temperature) (Matoza et al., 2009; Fee et al., 2013; Matoza et al., 2013). However, it is recognized that volcanic jet noise is more complicated than the case of human-made jet noise, since volcanic jet flows are multiphase and involve flow through complex vents that may also evolve with time during an eruption (Matoza et al., 2013). In this study we investigate these relationships empirically using field observations of a relatively small-scale volcanic jet flow: a fumarole.

In addition to being an analog to larger-scale volcanic jets, fumaroles are important to study in their own right. Fumaroles are a common outlet for volatiles at volcanoes, and changes in their activity may indicate changes in the volcanic system. From a monitoring perspective, detecting changes in fumarolic activity via infrasound, seismic, or a remote sensing method could provide critical information on the volcanic system in real-time. However, to use them in this capacity first requires a clear understanding between the geophysical signals they produce including detection and characterization. To date the work done towards characterization of fumarolic acoustics is an estimation of total acoustic power from gas jetting fumaroles by Woulff and McGetchin (1976).

A current goal of volcano infrasound research is to quantitatively relate recorded infrasound to the mass eruption rate of gas and tephra (Kim et al., 2015; De Angelis et al., 2016; Fee et al., 2017). Such quantitative relationships would greatly enhance hazard mitigation efforts through improved input parameters for plume modeling and near real-time estimates of erupted material. Recent work has pointed out that previously proposed connections between acoustic power and volcanic gas exit velocity (Woulff and McGetchin, 1976) are likely not valid for volcanic jet noise, and can lead to significant errors in eruption parameter estimation (Matoza et al., 2013). Matoza et al. (2013) suggested that the relationship between volcanic jet noise and flow parameters such as jet velocity should be empirically derived through experiments and comprehensive field observation. Human-made jet noise is highly directional with respect to angle from the jet axis; thus, sampling over this angular range is necessary to accurately characterize the sound produced by the jet. Matoza et al. (2013) highlighted a challenge in realistic volcanic environments: limited angular sampling of the acoustic wavefield since infrasound sensors are usually deployed on the ground surface.

Fumaroles are more accessible and less hazardous than large-scale volcanic jets in the form of Plinian eruption columns (Matoza et al., 2009; Fee et al., 2010a, Matoza et al., 2013); thus we investigate fumarole noise as a small-scale analog of large scale volcanic jet noise. Sound from fumaroles has previously been recorded and investigated using equivalent source theory (Woulff and McGetchin, 1976). In this study, we use campaign infrasound and thermal data to

characterize the acoustic signal from a gas-jetting fumarole at Aso volcano, Japan (Fig. 1). We also evaluate the fumarolic jet noise scaling and jet parameters and use an assumed Strouhal number to estimate volatile mass flux. Aso Volcano was selected for this investigation because recent activity included gas-jetting fumaroles and provided a location where we could sample natural jet noise at a smaller angle relative to most studies, which are typically >90° from the jet axis. Our ultimate aim is to improve the relationship between acoustics and volcanic jetting.

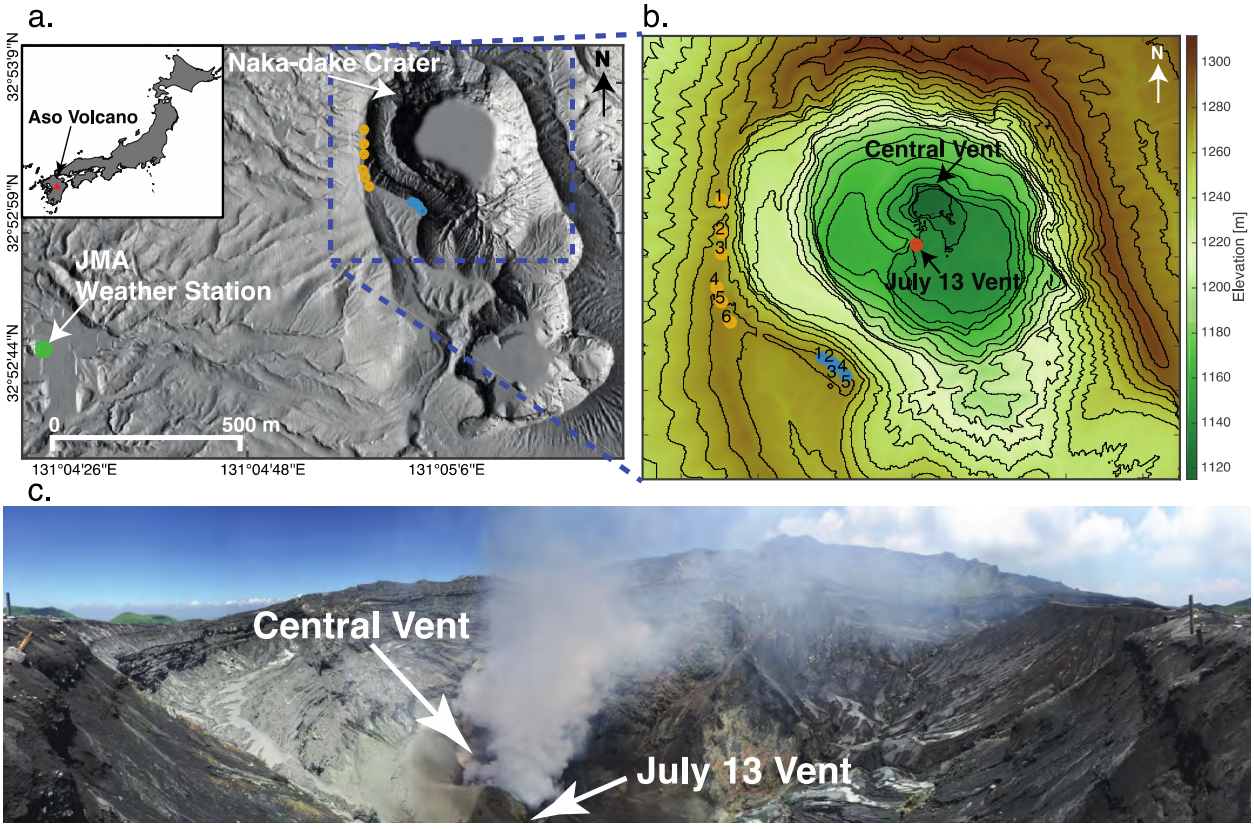

Figure 1. a) Location of Aso Volcano, Japan. Shaded relief map rendered from a 2012 1 m-resolution digital elevation model of the active summit of Aso volcano. The green circle highlights the location of the JMA weather station. The gold circles are the locations of the first array deployment on the western crater edge and the blue circles are the second deployment locations. b) Combined contour and shaded relief map of Naka-dake crater created by combining three 1 m-resolution DEMs. The central vent, July 13 vent (red circle), western array (gold circles) and southwestern array locations (blue circles) are shown. c) Panoramic photograph of Naka-dake crater taken ~10 m southeast of array element 5.

2. Background

2.1. Fumaroles

A fumarole is a vent in an active volcanic environment that issues steam and other volatiles (i.e. carbon dioxide, sulfur dioxide, etc.) at temperatures greater than 100°C (Allaby and Allaby, 2003). They are found at volcanic summits and flanks, and their gases are typically sampled to determine volatile species, ratios and flux as these hold information about the presence of magma at depth (Wallace, 2005; Fischer, 2008). Fumaroles are known to produce significant sound. Volcanologists often report audible jetting of volatiles from fumaroles. In seminal work, Woulff and McGetchin (1976) estimated the total acoustic power of fumarolic jets near the summit of Acatenango volcano, Guatemala using the power laws of Lighthill (1952). Lopez et

al. (in prep) report audible jetting of fumaroles at Mount Martin as far away at 16 km, which they suggest as an indicator of high pressure degassing. Matoza et al. (2010) recorded sustained, audible sound from a vent in a lava tube at Kilauea Volcano on several occasions with a nearby infrasound array, and likened the sound to jet noise. While the lava tube vent is not a fumarole as it is described as jetting gas and spattering lava, it is a relevant comparison as it could be another example of a smaller scale volcanic jet. The sound from the lava tube vent was predominantly in the 5-10 Hz band, which was higher in frequency than the infrasonic tremor from the Pu'u 'O'o crater. It was suggested that the frequency content was higher due to the smaller diameter of the lava tube vent. While regular observations are made that fumaroles produce jet noise, little work as of yet has characterized fumarolic sound with respect to jet noise.

2.2. Jet noise

A jet, whether human-made or natural, is the flow of momentum-driven fluid from a nozzle. Jet flow has three salient regions: core, transition and fully developed (Tam and Burton, 1984; Depuru Mohan et al., 2015). The core has nearly uniform fluid velocity with little turbulence. The transition region has a sharp drop in velocity from the jet axis outward and then self-similarity is reached in the fully developed region. The momentum-driven flow of a fluid into a quiescent fluid creates a velocity shear, which causes turbulence and mixing of the fluids (Kundu and Cohen, 2008). Turbulent jets can be conceptually decomposed into two components: fine-scale (FST) and large-scale (LST). The FST is randomly distributed eddies in the jet that are small relative to the jet diameter, while LST consists of coherent turbulent structure comparable in size to the jet diameter. Jet noise is the sound produced by the fluid flow downstream of the nozzle and is comprised of jet mixing noise, broadband shock associated noise, and screech tones (Tam, 1995), with FST and LST producing the two dominant components of jet mixing noise (Tam et al., 1996). Sound radiation from a jet is often characterized as a function of θ, relative to the jet axis and parallel to the overall jet flow (Fig. 2). LST noise is generally strongest in the downstream direction at small angles (~20° – 40°) in a cone about the jet axis. FST noise is typically dominant at higher angles (~60° – 96°), further upstream from the nozzle (Tam et al., 1996). In other words, jet noise is highly directional (Tam and Chen, 1994). Jet mixing noise spectra are broadband with power decay away from a broad peak frequency. FST and LST noise spectra both have a peak and fall-off in power at high and low frequencies away from the peak, but with different spectral shapes (Tam, 1995; Tam et al., 1996; Tam, 1998). The LST spectrum is narrower while the FST spectrum is broader (Tam et al., 1996). A key characteristic of jet flows is their self-similarity, meaning jets have geometric, kinematic, and dynamic scaling and scale through time (Pritchard, 2011). Geometric scaling or similarity means if the nozzle diameter is increased then the length scale of the other jet components will increase by the same scaling factor while preserving all angles and flow directions. Kinematic scaling is when velocities at corresponding points have the same direction and their magnitudes have a constant scale factor. Dynamic scaling is met when the forces are parallel and are related by a constant scale factor. Since jet flows are self-similar, jet-noise is also proposed to be self-similar (Tam et al., 1996). This means that while experimental and human-made jets may range from centimeter to meter scale, the same features have been observed and in turn the recorded sounds have a similar spectral shape. For supersonic jets, the downstream movement of LST at supersonic speeds is considered the source of sound (Tam et al., 2008). However, for subsonic jets the growth and decay of LST at supersonic speeds perturbs the atmosphere to create acoustic pressure waves (Viswanathan, 2009). Jet noise is typically identified by its frequency content,

features such as crackle for supersonic jets, and its distinct audible signature (Tam, 1995; Tam et al., 1996; Tam, 1998).

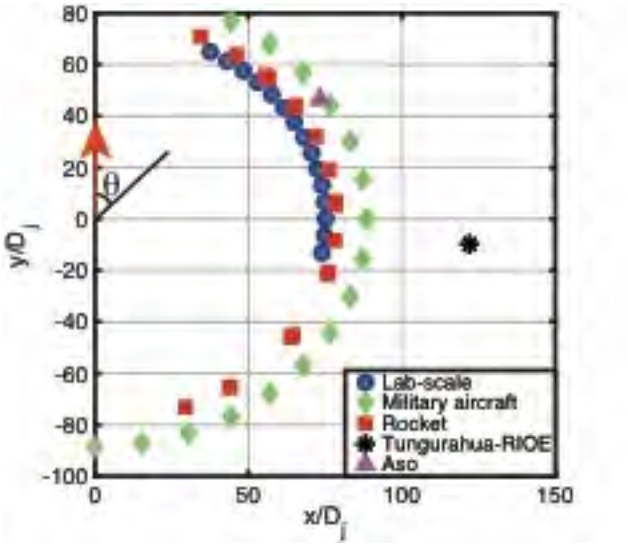

Figure 2. Comparison of acoustic observation angles and distances for lab-scale (blue circles), military aircraft (green diamonds), rocket engines (red squares), volcanic (Tungurahua-RIOE, black asterisk), and Aso fumarolic (purple triangle) jets. The x and y distances are scaled by the jet nozzle diameter, D_j. The nozzle is at (0, 0) and flows in the direction of the orange arrow. The black line highlights the angle θ relative to the jet axis. Figure modified from Matoza et al. (2013).

Volcanic jet noise from sustained sub-plinian and plinian eruptions has been observed to be high-amplitude, long-duration, emergent and broadband (Matoza et al., 2009; Fee et al., 2010a; Fee et al., 2010b). Jet noise from volcanoes spans infrasonic to audible frequencies, as audible jetting was noted at Karymsky volcano, Kamchatka (Lopez et al., 2013; Rowell et al., 2014). Volcanic jet noise is thought to be predominantly comprised of jet mixing noise. Broadband shock and screech tones are unlikely to be produced by volcanoes because of the natural, dynamic elements of a volcanic jet: irregular nozzle, tephra, and changing vent shape (Matoza et al., 2009). Taddeucci et al. (2014) recently observed high-frequency jet noise at Stromboli volcano, which may be related to shock waves emanating from the jet. Recent work has compared the PSD curves (Matoza et al., 2009) and skewness of the waveform probability density functions (Fee et al., 2013; Goto et al., 2014) of human-made jet noise with volcanic jet noise; this is possible because of the self-similarity of jets and jet noise. To compare different jet noise spectra the Strouhal number, *St,* is used. It is a dimensionless number of the form $St = \frac{fD_j}{U_j}$, where f is the peak jet frequency, D_j is the expanded jet diameter and U_j is the jet velocity. The Strouhal number is valuable for the analysis of unsteady, oscillating fluid flows, such as from jets. Comparison of human-made and volcanic jet spectra can be performed by evaluating the Strouhal numbers of the flows, assuming that both types of flows have a peak Strouhal number. Tam et al. (1996) observed that as jet velocity decreased toward ambient sound speed the Strouhal number asymptotically approaches a constant of ~0.19, independent of jet temperature. Some estimates of Strouhal numbers of volcanic jet flows have been made at Tungurahua, Ecuador: 0.4, and Mount St. Helens, USA: 0.06 (Matoza et al., 2009) and numerically modeled at 0.4 (Cerminara et al., 2016).

2.3. Aso Volcano

Aso Volcano, one of Japan's most active volcanoes and a popular tourist destination, is located in central Kyushu, the southern-most of the four main islands of Japan (Fig. 1a insert). It is an 18 x 25 km caldera with current activity focused at the northernmost crater of a north-south trending line of craters (Fig. 1a) (Kaneko et al., 2007). Figure 1 shows a map view into the active crater at Naka-dake summit (Yokoo and Taniguchi, 2004; Takagi et al., 2006). From the southwestern rim, the crater is about 115 m deep with near vertical walls. Historic eruptions have consisted of basaltic to basaltic-andesite ash emissions with periods of strombolian and phreatomagmatic activity (Kaneshima et al., 1996). After a 22 years hiatus, eruptive activity returned in November 2014 and lasted for 6 months. Figure 3a shows an image of the crater taken in 2011 with two distinct degassing areas: the center and the south-southeast crater wall. This eruptive period included periods of strombolian to vulcanian, ash-poor to ash-rich explosions; gas jetting; and fumarolic degassing (Yokoo and Miyabuchi, 2015). Deposits from repeated strombolian explosions built a pyroclastic cone within the active crater (Fig. 3b,c). At its maximum in March 2015, the cone was ~20 m in height and had a ~200 m diameter at the base. On 3 May 2015 part of the cone collapsed into the central vent ending the strombolian activity. From this point, the central vent degassed without any ash and began to fill with water. On 13 July 2015 a new small vent opened at the edge of the partially collapsed pyroclastic cone, highlighted by the red circle and named July 13 vent in Figure 1b. The July 13 vent is considered to be a large fumarole as it issued steam and other volatiles with no evidence of ash (Fig. 3c,d). The SSE wall fumaroles in Fig. 3a-c have been present for years, contribute to the total volatile flux, are not vigorous (Mori, 2012; Shinohara et al., 2015), and do not seem to produce audible or low frequency sound.

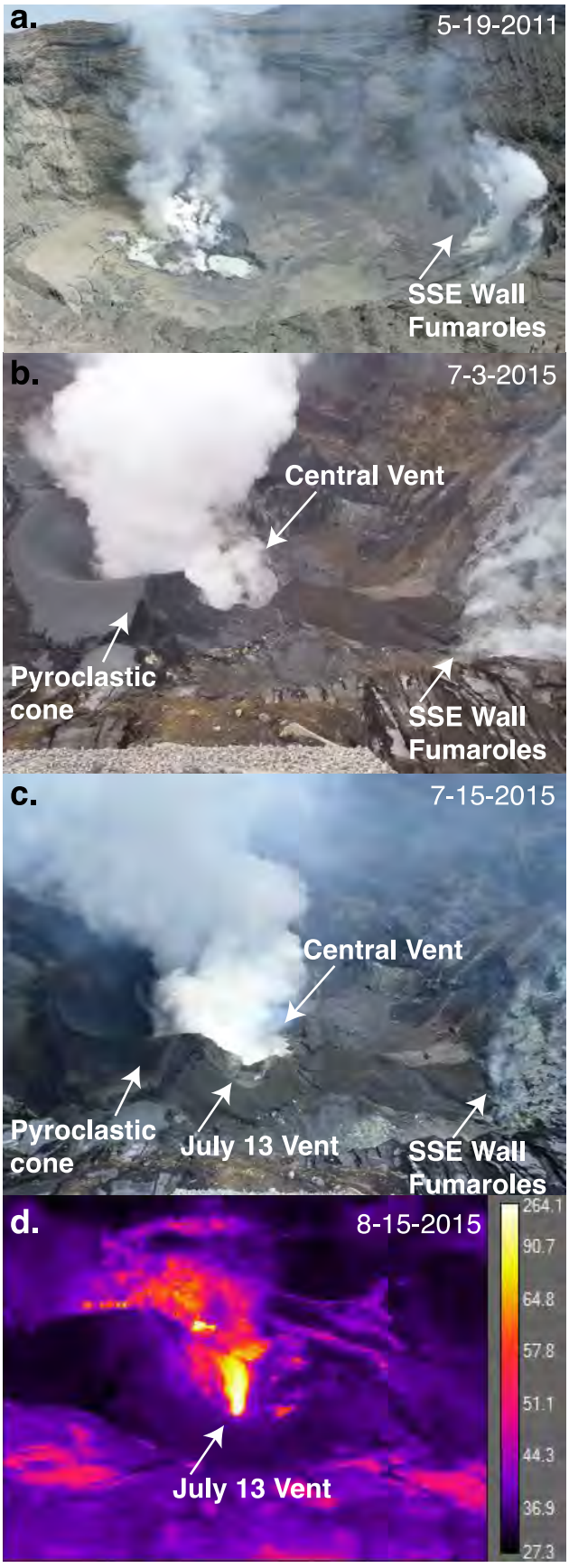
a.
5-19-2011
SSE Wall
Fumaroles
b.
7-3-2015
Central Vent
Pyroclastic
cone
SSE Wall
Fumaroles
c.
7-15-2015
Central Vent
Pyroclastic
cone
July 13 Vent
SSE Wall
Fumaroles
d.
8-15-2015
July 13 Vent
264.1
90.7
64.8
57.8
51.1
44.3
36.9
27.3

221

Figure 3. Images of Naka-dake crater from a) 2011 and b), c) and d) 2015. a-c) show the activity at the center of the crater and the fumaroles on the southeastern crater wall. c) Visible and d) thermal infrared images of the July 13 vent with steam plume rising from the central vent in the background. The warm spots in the foreground are due to correcting the entire TIR image by the distance from the camera to the July 13 vent. Images were taken from the southwestern array location.

Aso Volcano was selected for this research project for several reasons. First, it is an accessible (i.e. road and cable car) volcano with both audible jet noise and continuous, vigorous degassing as observed by the scientists of the nearby Aso Volcanological Laboratory (AVL). This type of activity and access is unusual. Second, given the activity and access it is a relatively safe environment to work compared to more hazardous eruptions. Finally, the topographic setting at Aso allowed for unique sensor locations such that the microphones were deployed above the fumarole at a smaller angle to the jet axis than previously achieved in volcano studies (Matoza et al., 2009; Rowell et al., 2014).

3. Data

In July 2015 we deployed a 6-element array of infrasound sensors along the western rim of the active crater of Aso (Fig. 1a,b). The microphones, referred to as Volcano Differential Pressure (VDP) sensors, (Thelen and Cooper, 2015) had a sensitivity of 10 mV/Pa. The sensors have a flat response between 0.0125-25 Hz and data were recorded on a 6-channel Geotech SMART-24 digitizer at 250 Hz, permitting sampling of both the infrasonic and lower audible frequency range. Sensor responses were verified in huddle tests before and after the experiment. The array was initially deployed along the western crater rim to get as much azimuthal coverage as possible relative to the permanent infrasound network run by AVL.

During the deployment the aforementioned July 13 vent opened at approximately 17:00 UTC 13 July 2015, and is shown in visible and infrared images in Figure 3c,d. The local, permanent seismoacoustic network did not detect the opening of the fumarolic vent, nor did the temporary acoustic array on the western crater rim. AVL observed its presence with the local web camera. When in the field, standing where the July 13 vent was visible, this vent clearly produced audible sound akin to jet noise. However, this audible noise was not heard on the west rim of the caldera where the array was located, nor was coherent sound detected in initial processing of these data. Therefore, we moved the array to the southwestern rim to better capture the sound produced by the July 13 vent. The array was at the western rim from 3 July to 3 August 2015 and at the southwestern rim from 3 - 13 August 2015. Figure 1b shows the locations of the second array location, central vent and July 13 vent. While at this location, the array was 216.9 meters from the July 13 vent and positioned 57.6° from the vertical jet axis, a recording angle usually not feasible in volcanic environments. The inter-element spacing was about 10 meters, with five sensors aligned along the crater rim. The July 13 vent was visible from elements 2-5 but not from element 1, as the crater rim topography blocked line-of-sight.

In addition to the infrasound data, four thermal infrared (TIR) images were captured just after the deployment period by AVL. A FLIR T440 camera was used to take images at the locations of array elements 1, 2, 3 and 5 on 16 August 2015 (Fig. 3d). Note the fumarolic vent was not visible from array element 1, but the heat from the jet was observed in thermal IR. AVL shared five digital elevation models (DEM): two of the Aso summit region at 1 m (Figure 1a) and 5 m resolution and three of Naka-dake crater at 1 m resolution (Figure 1b). The crater DEMs were

collected in March 2015, May 2015 after the cone collapse using an unmanned aerial vehicle, and August 2015 using reconstructed photographs taken on a circumnavigation of the crater rim.

4. Methods

To characterize the acoustic signal of Aso's gas jetting fumarole, array-processing methods are applied to determine times of coherent signal. We use the Mean of Cross-Correlation Maxima (MCCM) method as it has been shown to be a robust detector even when the signal-to-noise ratio is low (Lee et al., 2013). To determine times of coherent acoustic signal with MCCM, data are band-pass filtered in frequency bands of interest and then unique sensor pairs are cross-correlated through time with appropriate window lengths relative to signal period. The mean of the peak cross-correlation values for each time window is then taken as the MCCM. For the data recorded at Aso, we use three different frequency bands and a complementary, non-overlapping window length: 0.5 to 5 Hz with a 10 s window, 5 to 15 Hz with a 5 s window, and 15 to 25 Hz with a 2 s window. A 0.5 Hz lower bound was chosen to remove the microbarom influence. The 25 Hz upper limit was selected because topography and other propagation effects increasingly influence shorter wavelengths. An MCCM value of 0.8 or higher was considered indicative of coherent acoustic signal. During the first 4 weeks of the deployment, when the array was on the western rim, no correlated signals were found. The crater rim had high winds during the site visits and the sensors did not have any wind noise suppression installed. To then describe the acoustic characteristics of the fumarole time series, spectrograms and power spectral density (PSD) curves were analyzed for 30+ minute windows where MCCM values were greater than 0.8. The PSD curves were smoothed once for ease of comparison using a triangular window.

The effects of path to acoustic wave propagation include power loss from increased path length and altering the waveform due to reflections. Recent work has shown that topographic path effects significantly contribute to the recorded acoustic waveforms in volcanic environments (Lacanna and Ripepe, 2013; Fee et al., 2014; Kim and Lees, 2014), and that to account for it, 3-D numerical modeling should be incorporated (Kim et al., 2015). Acoustic waves diffract or bend around obstacles in their path such as topographic structures. This increases the path length and decreases the recorded amplitude compared to a wave with the same source-receiver distance without an obstacle. Recent work has also shown that as acoustic waves diffract around the crater rim of a volcanic edifice the waveform shape is altered, particularly the initial rarefaction (Kim and Lees, 2011; Lacanna and Ripepe, 2013). For the frequency bands used in our analysis, the corresponding wavelengths range from 13.6 m (25 Hz) to 680 m (0.5 Hz) at a sound speed of 340 m/s. As the crater wall is about 115 m high on the southwestern side and within the range of our wavelengths of interest, it will likely influence the recorded waveforms. Reflections from Aso's crater may also be significant and should be considered. To account for topographic path effects we computed the numerical waveforms in three dimensions using the finite difference time domain (FDTD) method of Kim et al. (2015), which incorporates a high-resolution DEM. We assumed a homogeneous atmosphere (density = 1.16 kg/m^3, sound speed = 346 m/s) for numerical simulations as the variation of the speed of sound and air density should be small and their influence on sound propagation minimized at the distances considered here (Johnson and Ripepe, 2011; Kim and Lees, 2014; Kim et al., 2015).

We merged two high resolution DEMs of Naka-dake crater for the synthetic data calculation and to determine a more accurate location of the July 13 vent. This merge was necessary because the

May 2015 DEM did not contain the July 13 vent and the August 2015 DEM had skewed elevations at the walls due to the acquisition method. The resulting DEM is shown in Figure 1b.

The determination of the jet parameters, specifically the jet diameter, temperature and gas exit velocity, are necessary to facilitate jet noise comparison. We determine the jet diameter and temperature by analyzing infrared thermal images. The raw thermal images were corrected for distance (216.9 m), air temperature (21.1°C) and local relative humidity (87%) by inputting those parameters into the ResearchIR software. Local air temperature and relative humidity data are from the JMA weather station (Fig. 1a). There is uncertainty in using these values as the weather station is not at the Naka-dake crater rim, but we do not expect the differences to significantly affect the results. The default emissivity value (0.95) in ResearchIR was used, as an emissivity value could not be found for water vapor or any other gas. However this value is likely too high as theory suggests pure hot gas emissivity is <0.2 and invisible in TIR (Yokoo et al., 2013). The jet diameter is determined by first computing the pixel dimensions in physical space at the July 13 vent. The thermal images are 320 x 240 pixels with a field of view of 25° x 19°. The dimension of a pixel is $x = \left(2d\tan\frac{\alpha}{2}\right)/n_x$ and $y = \left(2d\tan\frac{\beta}{2}/n_y\right)$, where d is the distance from the location the image was taken to the location of a pixel in physical space, α and β are the field of view for a given camera, the FLIR T440 in this case, in the x and y dimensions, and n_x and n_y are the number of pixels in horizontal and vertical dimensions of the image, respectively (Lillesand et al., 2008). The hottest pixel in each image is assumed to be the center of the fumarolic vent. The dimension of the hottest pixel in each image is approximately 0.3 x 0.3 m, giving an estimate of the hottest pixel resolution at the fumarolic vent. As the vent in the images used is ~8 pixels across, we assume the dimensions of the hottest pixel is an appropriate approximation for all the pixels near it. We then take a temperature profile from left to right across the images through the hottest pixel. The average width of the temperature peak in the profiles from array elements, 2, 3 and 5 was taken as the jet diameter. The TIR image taken from array element 1 was not used, as the vent was not visible from that position. The average temperature of the hottest pixel from the same three images was used as the jet temperature. To compare different jets we estimated the jet temperature ratio, T_j/T_a, where T_j is jet temperature and T_a is ambient temperature.

Once the jet temperature and peak spectral frequency are determined, the Strouhal number is used to estimate the jet velocity. Assuming the fumarolic jet noise is comprised of mostly jet mixing noise and behaves similar to human-made jets (Matoza et al., 2009), we use a Strouhal number of 0.19 and calculate velocity by $v = \frac{f \times D_j}{St}$, where f is the peak frequency selected from the PSD curves and D_j is the jet diameter determined from the temperature profiles. Like the temperature ratio, another key ratio for comparing jets is the velocity ratio, v_j/v_a, where v_j is the jet velocity and v_a is the speed of sound. This ratio is known as the Mach number, M. A jet with $M < 1$ is labeled subsonic and $M > 1$ is supersonic. Once the jet velocity is estimated, the volatile flux, j_v, is estimated by $j_v = \rho v_j A$, where ρ is the density of the volatiles, v_j is estimated jet velocity, and A is fumarolic vent cross-sectional area. To estimate volatile density in the jet, we used gas composition data in Table 1 of Shinohara et al. (2015), collected at Aso from fumaroles over a five year period, 2004 – 2009. They published gas concentrations in μmol/mol

for the following species: H_2O, CO_2, SO_2, H_2S, HCl, HF, and H_2. The gas concentration from 16 samples were averaged and then converted to density using the ideal gas law. For example, the volume can be calculated by converting 980,000 ppm H_2O to 980,000x10^{-6} m^3 H_2O per 1 m^3 air. We then calculate the number of moles, n, using $n = PV/RT$, where P is the atmospheric pressure at Naka-dake crater's elevation 1159.9 m above sea level (88563 Pa), V is the volume (0.98), R is the ideal gas constant (8.31441 Pa/K•mol), and T is the gas temperature estimated from the thermal images. The number of moles, n, is then multiplied by the molecular weight of water, 18.02 g/mol, which gives the H_2O density, ρ_{H_2O}. This is repeated for each volatile species and then the densities are summed to get the total volatile density, ρ_T. The total volatile density (kg/m^3) is then multiplied by estimated jet velocity (m/s) and vent area (m^2) to estimate total volatile mass flux (kg/s).

5. Results

5.1. Signal Detection

MCCM analysis of the dataset revealed periods of acoustic signal from Aso's July 13 vent, as well as extensive periods of high noise (wind). Hours to days of correlated signal are detected during the 10 days the array was deployed in the second location, although strong winds still influenced the detections. Figure 4a shows six hours of array acoustic data and Figure 4b the peak cross-correlation values through time for each of the unique sensor pairs. The peak pressure for each trace is listed to the left and highlights the low amplitude of the signal, typically <1 Pa. Infrasonic amplitude decays at a rate of 1/*r*, where *r* is the distance from the source. To compare pressure amplitudes, the pressures are reduced to a reference distance, r_{ref}, usually 1 or 1000 m from the source, by simply multiplying the pressure by r/r_{ref} distance (Johnson and Ripepe, 2011). Infrasonic tremor from the Halema'uma'u Crater of Kilauea Volcano has pressures of ~477 Pa when reduced to 10 m (Fee and Matoza, 2013), which is orders of magnitude larger than the jet noise recorded at Aso (~6 Pa when reduced to the same distance). Figure 4c-d, similar to Figure 4a-b, highlights times with larger amplitudes where the traces appear visually similar, but the correlation values are low. This suggests the presence of wind noise as the array elements were spaced far enough apart to reduce wind noise correlation (Walker and Hedlin, 2009). Figure 5a, c, and e shows the MCCM values for the second array location for three different frequency bands over a span of 9 days and Figure 5b, d, and f shows the times series data from array element 3 for the respective frequency bands. The red dots indicate MCCM>0.8. Hours to days of correlated signal in the 0.5 to 25 Hz band are present. Figure 5g shows the wind speeds recorded at a Japan Meteorological Agency (JMA) weather station ~1 km from Naka-dake crater (Fig. 1a). This figure shows that when the wind speed increases, the MCCM values in the three frequency bands drop significantly.

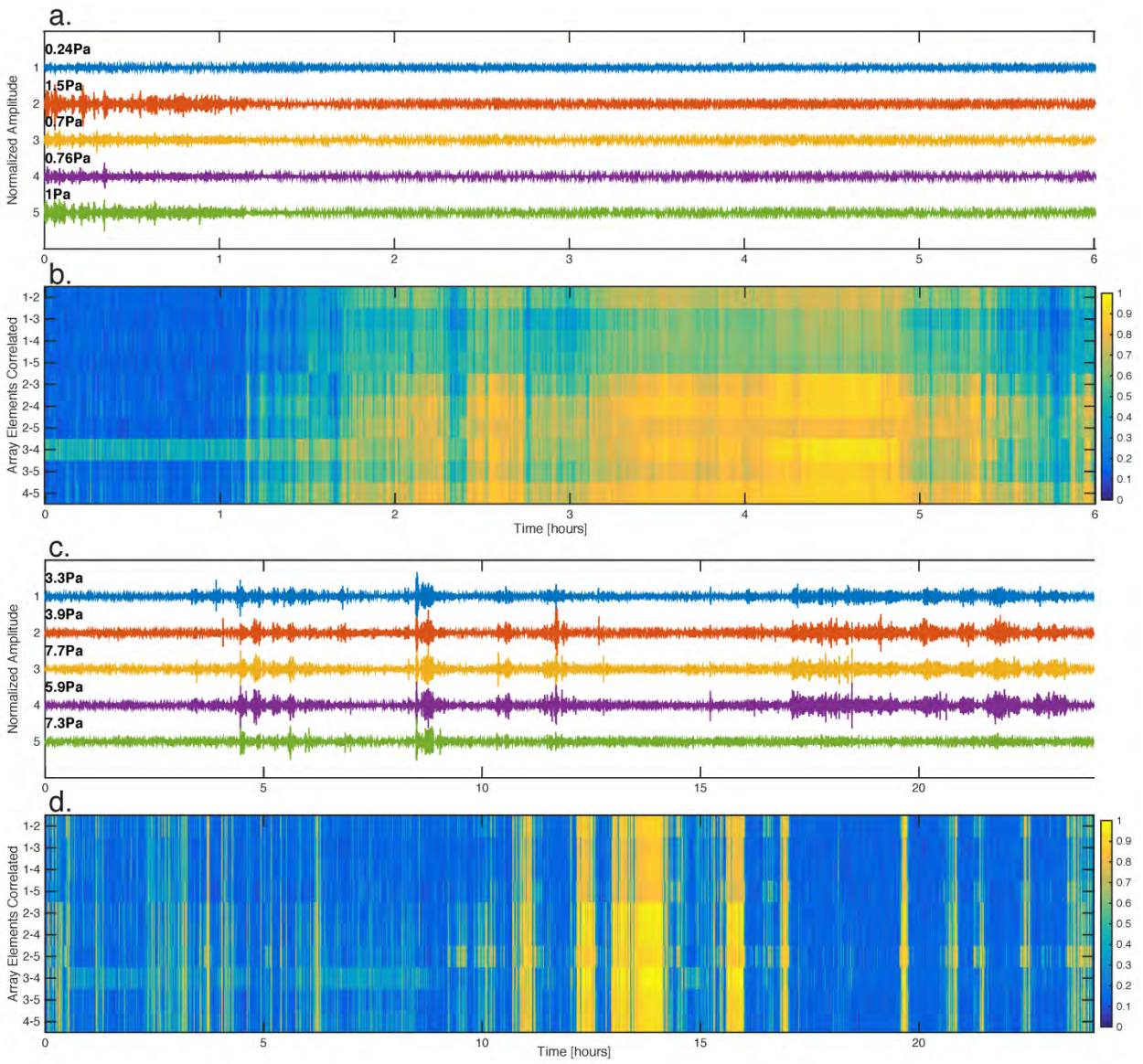

Figure 4. a) 6 hours of normalized acoustic data from array elements 1 – 5 starting on 4 August 2015 at 17:30 UTC. Data were filtered from 0.5 to 5 Hz. Peak amplitude for each trace is listed at the left. b) Each row represents the peak cross-correlation values though time for each sensor pair in the array. Filtered data from unique element pairs were cross-correlated using a 10-second non-overlapping moving window. c) and d) show time series data and peak cross-correlation values through time as in a) and b), but for 24 hours of data starting on 08 August 2015 at 00:00 UTC.

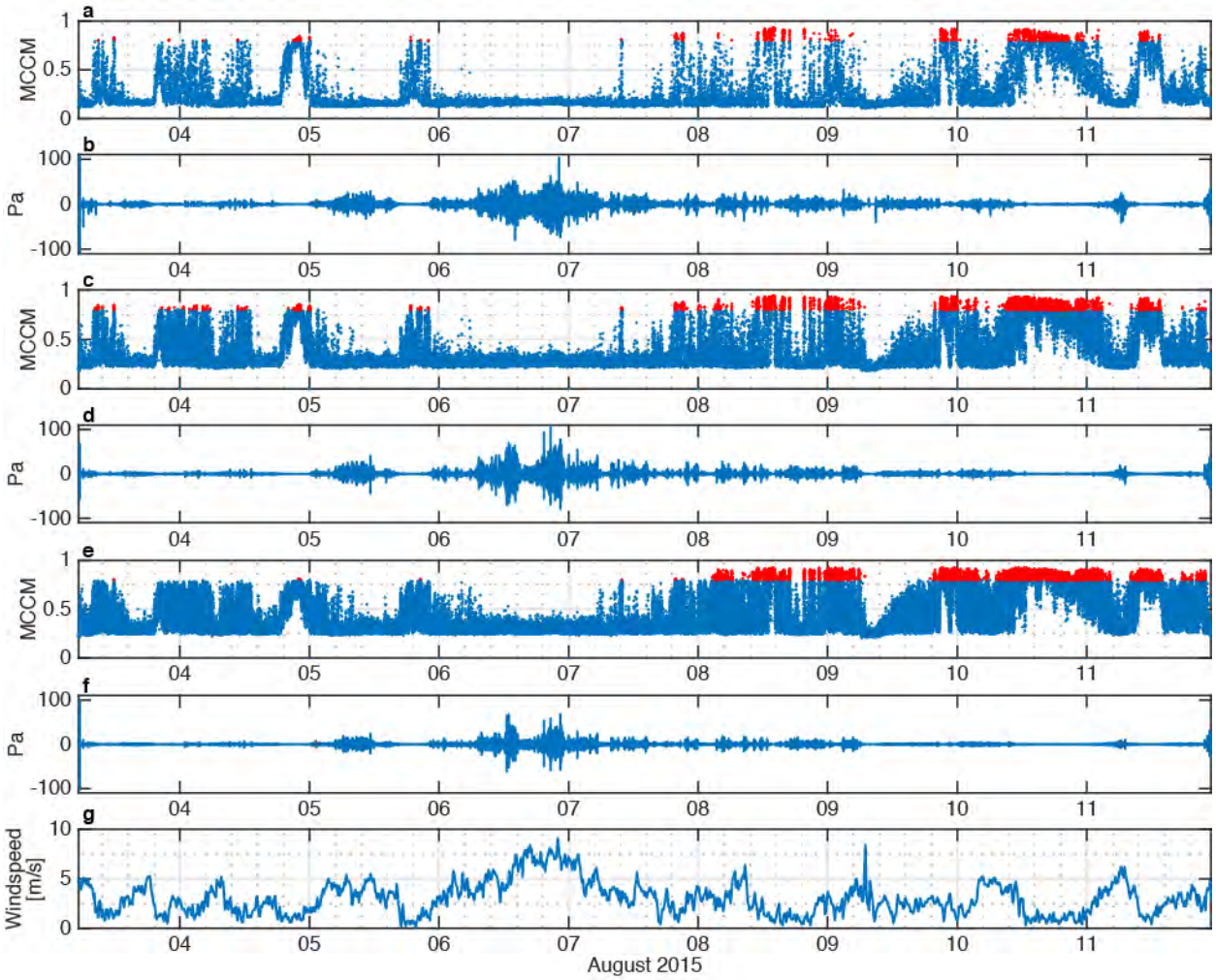

Figure 5. Mean cross-correlation maxima (MCCM) and waveforms from array element 3 from 3 – 11 August 2015 for three different frequency bands: a) MCCM filtered from 0.5 to 5 Hz with a 10-second window and b) waveforms; c) 5 to 15 Hz with a 5-second window and d) waveforms; and e) 15 to 25 Hz with a 2-second window and f) waveforms. Red dots indicate MCCM > 0.8. g) 10-minute averaged wind speed data recorded at a Japan Meteorological Agency weather station ~1 km southwest of Naka-dake crater (Fig. 1a).

5.2. Spectral Analysis

We analyze the spectra to help identify jet noise from the July 13th fumarole. Figure 6a, b and c shows the time series and spectrogram data from element 3, and PSD curves from sensor 1 to 5, respectively, for 30 minutes of data on 4 August 2015 with MCCM values above the threshold. Figure 6d, e and f are similar, but for a 30-minute window recorded on 8 August 2015. The pressures for both of these have been reduced to 10 m from the source as described previously. These two time series examples show persistent tremor that does not change over the duration shown. The spectrograms show this tremor to be predominantly below 20 Hz, but also present up to 60 Hz. The PSD curves further illustrate the broadband nature of the signal as the power decays linearly to about 1 Hz, then increases at 2 Hz and decays over a broad curve in to the higher frequencies. The signal is low-amplitude, especially compared to the wind noise (Fig. 4c), as the amplitude is on the order of 0.1 Pa at ~220 meters from the source. It is sustained for hours to days with peak frequencies ranging from 2 to 10 Hz. Figure 6c shows a time when the peak frequency is 2-6 Hz and in Figure 6f it is about 6-10 Hz; the latter is more commonly observed in

our dataset. We note there is significant structure and differences in power in the PSD curves, particularly at frequencies greater than 10 Hz.

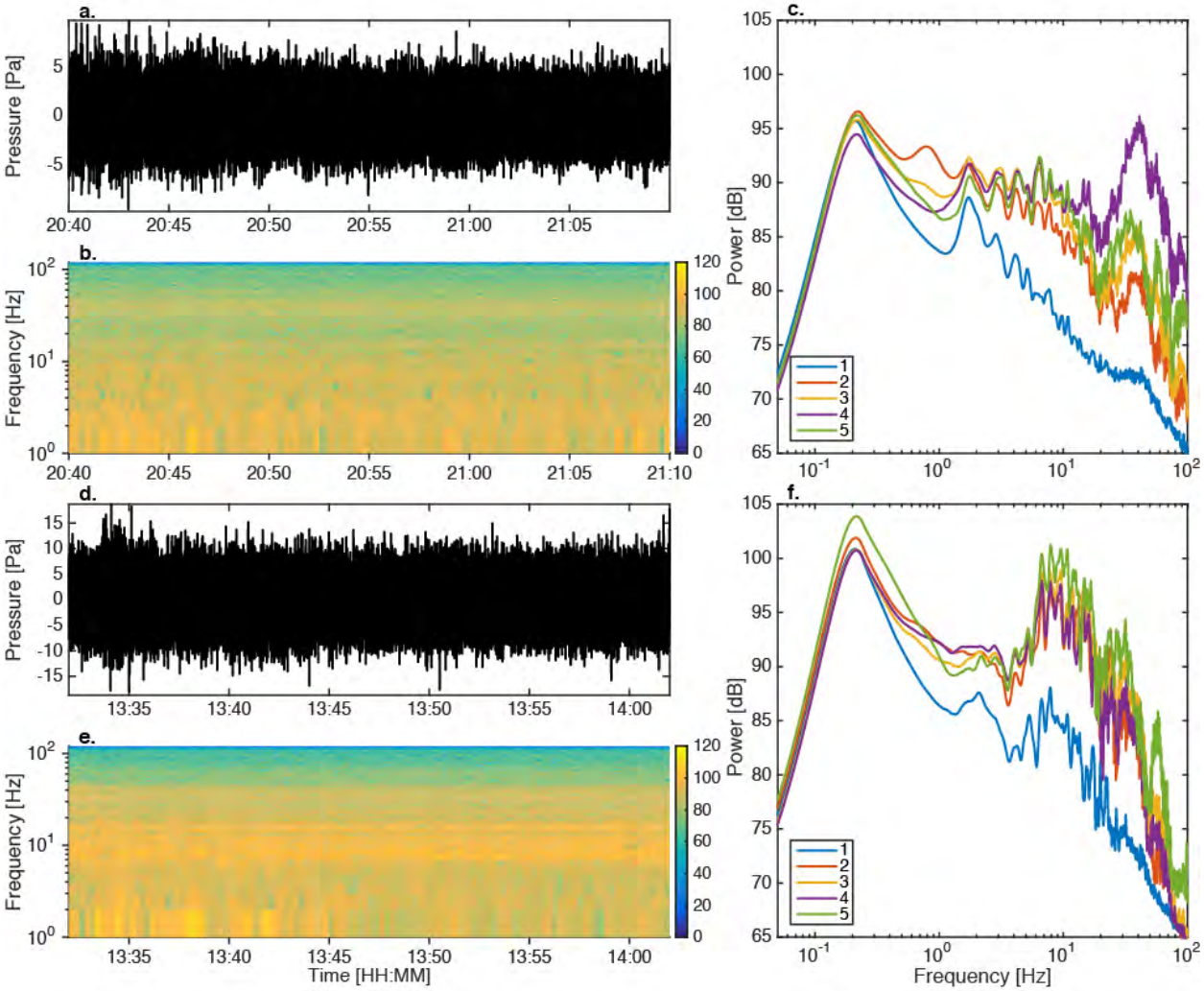

Figure 6. a) 30-minutes of times series data and b) the corresponding spectrogram from array element 3 on 4 August 2015 starting at 20:40 UTC. The pressure has been reduced to 10 m from the fumarolic vent. c) Smoothed power spectra for the same 30-minute window of data for array elements 1 – 5. d), e), and f), show the same information as a), b), and c), respectively for 30 minutes of sound recorded on 8 August 2015 starting at 13:32 UTC.

5.3. Path Effects

Figure 7 shows the topographic profiles from each array element to the fumarolic vent to investigate acoustic propagation and local path effects. We note two items in the topographic profile that may be relevant to the acoustic propagation: 1) the crater wall is a significant feature, ~115 m high, on the same order of the acoustic wavelengths of interest and 2) the crater wall does not change significantly between the profiles aside from a small perturbation in profiles 1 and 2 just around 100 m between the sites and vent.

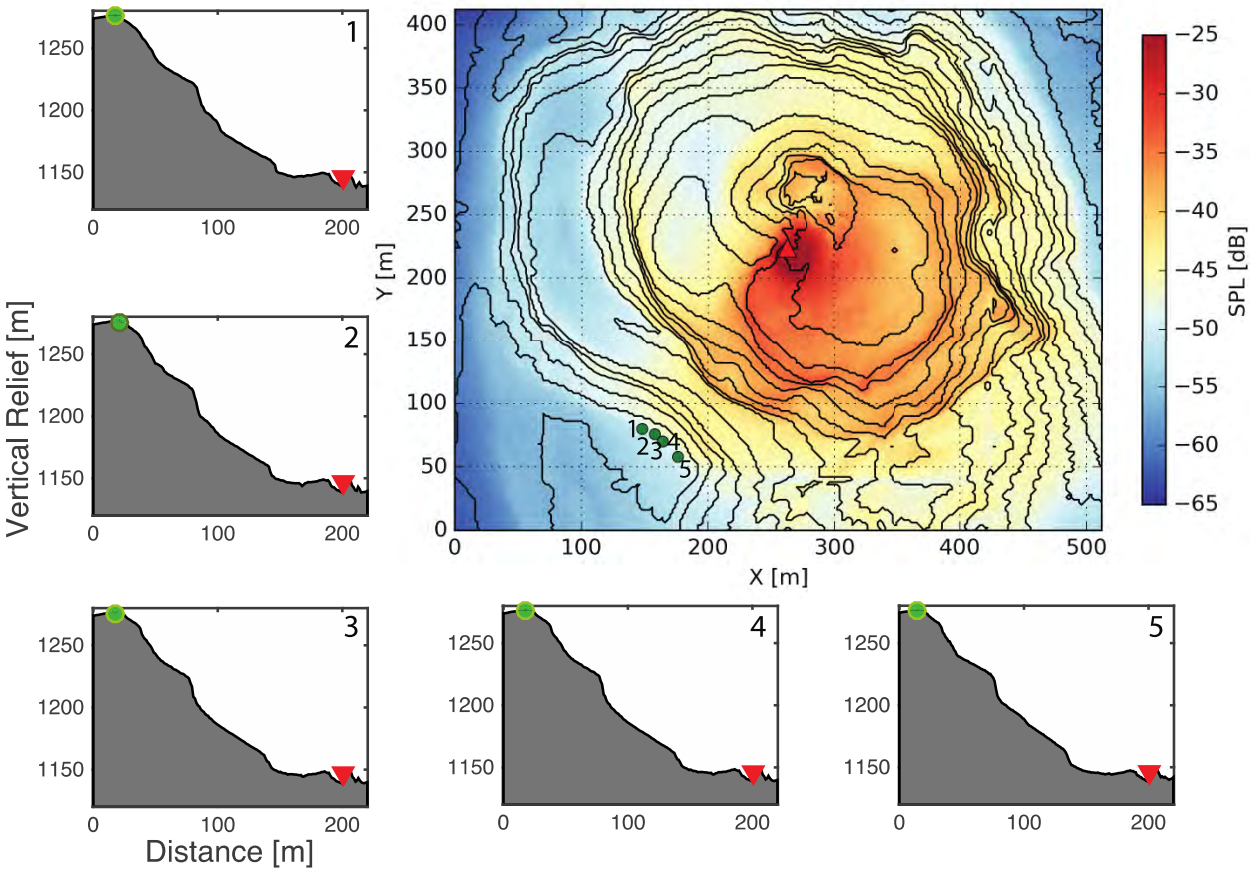

Figure 7. Topographic profiles and Sound Pressure Level (SPL). Topographic profiles 1 – 5 are from array elements 1 – 5 (green circles), respectively, to the fumarolic vent (red triangles). The five profiles correspond to the five array elements (green circles) in the central contour map. The contour map of Naka-dake crater is overlain with the total SPL loss for the 4-second SW computation. The red triangle is the location of the fumarolic vent and the point where the source time function is inserted. Array elements 3 and 4 were deployed next two each other and thus appear as a single circle. As the colors approach blue they represent lower sound levels (hence greater sound loss).

Synthetic waveforms, SWs, were computed by the FDTD method to further investigate spectral properties of the observations and influences of acoustic propagation (i.e. topographic propagation effects). We use a simple, impulsive, broadband source (blackman-harris window function) to excite acoustic wavefields in the modeling (Kim et al., 2015). Figure 8 shows the synthetic source and subsequent SWs. Note that the purpose of this numerical simulation is to generate "pseudo" Green's functions to understand propagation effects on sound propagation effects on sound amplitudes and spectral properties, but is not to reproduce the observed signals. Actual acoustic sources for fumarolic activities should be more complicated than a simple impulse used here. From array element 5, the southeastern most, to 1, the northwestern most, there is increasing loss in amplitude. This loss is reflected in the spectra as well. Figure 9a shows the power spectra for the SWs using Thomson's multitaper method due to the small number of data points. Details of this method are found in Thomson (1982) and Prieto et al. (2007). The source spectra have been deconvolved from the SWs spectra. Figure 9b shows the power difference relative to the first array element. For this plot, the spectrum from SW for element 1 was subtracted from the spectra for SWs for array elements 1 – 5. There is little difference in the SWs spectral power below about 3 Hz above which the differences are about 1 to 3 dB. The

power difference between any given array element and element 1 are not consistent across frequencies. For example, at about 4 Hz the difference between elements 1 and 5 is over 3 dB, while at about 5 Hz it is <1 dB. The structure in the SWs spectra is similar across the array elements up to about 6 Hz at which point they vary. Figure 7 shows the total sound pressure level (SPL) for an impulsive source initiated at the fumarolic vent, indicated by the red triangle, and propagated out for 4 seconds. Significant near-source directionality is present in this figure, as the SPL is highest to the south and southeast of the source, with significant loss to the northwest.

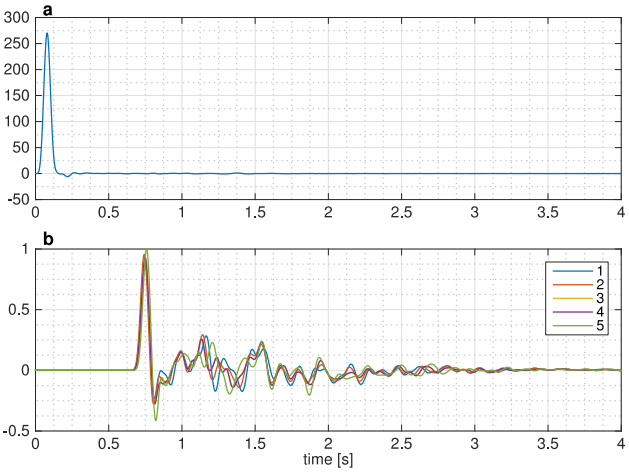

Figure 8. a) The source function for computing the synthetic waveforms. b) are the synthetic waveforms for array elements 1 – 5. The source time and SWs have been normalized by the maximum value in the SWs.

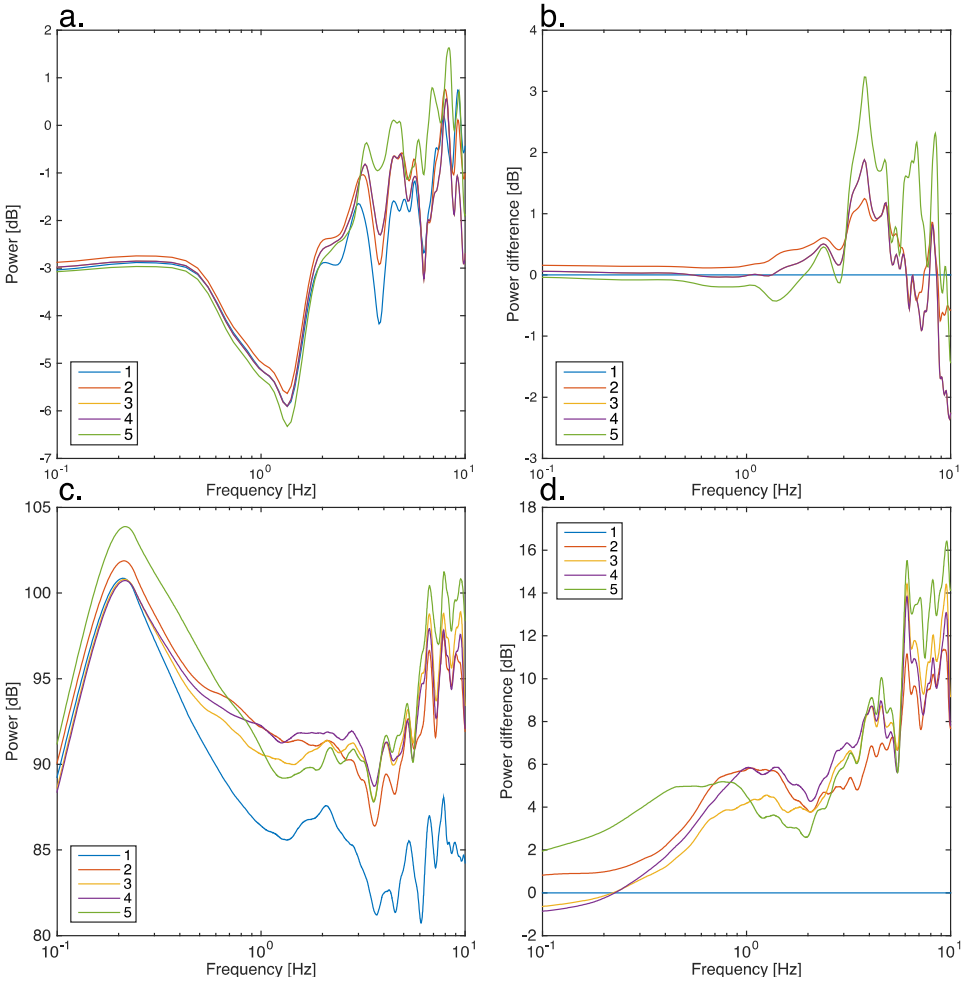

Figure 9. a) Power spectral density curves for the SWs using the multitaper method. b) Power difference relative to array element 1 SW. c and d) are the smoothed power spectra and power differences relative to array element 1 for the same 30 minutes of data from Figure 6d,e and f.

5.4. Volcanic Jet Parameters and Volatile Mass Flux

Volcanic jet diameter and velocity are derived using infrared and acoustic data, respectively. Figure 10 shows a corrected infrared thermal image from a FLIR camera at ~220 m distance and the corresponding temperature profile. The inferred jet diameter and temperature are ~2.5 m and ~260°C, respectively. We estimated the fumarolic jet velocity to be 79 to 132 m/s based on the more commonly observed range of peak frequencies, 6 – 10 Hz (Fig. 6) and the assumed St=0.19. The average air temperature during the second array deployment was 21.8°C from the local JMA weather station. This results in a temperature ratio of 11.9; a temperature ratio above 1 indicates the jet is hot. The speed of sound given the local average air temperature is 344.5 m/s. This gives a range of Mach numbers from 0.3 to 0.4, where a Mach number less than 1 indicates the jet is subsonic.

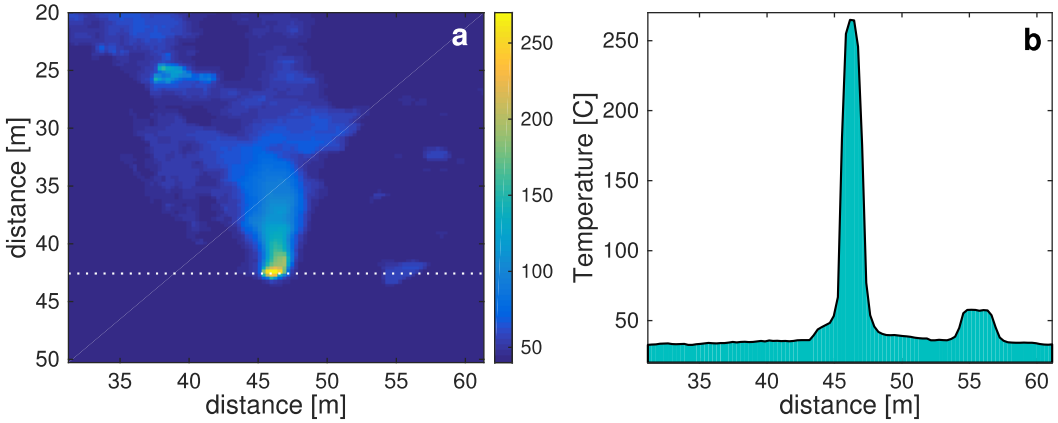

Figure 10. Thermal infrared (TIR) observations. a) TIR image captured on 14 August 2015 of the fumarolic vent from array element location 3. The dotted white line is where the temperature profile was taken. b) The temperature profile taken from left to right across the hottest pixel from the TIR image a.

Volatile flux (Table 1) is estimated using the estimated jet temperature, diameter and velocity, and volatile concentrations from Shinohara et al. (2015). For the flux estimations in Table 1, the jet velocity ranges from 79 to 132 m/s and the vent area is 4.91 m^2, assuming the vent is circular. Water is the most abundant volatile of the total at 11,000 to 18,000 tonnes/day and the SO_2 mass flux is 850 to 1400 tonnes/day.

Volatile Species	Mean Concentration	Molecular Mass	Density	Estimated Flux	Estimated Flux
	[µmol/mol]	[g/mol]	[g/m^3]	[Kg/s]	[tonnes/day]
H_2O	920000 ±32000	18.02	331	130 - 210	11000 - 19000
CO_2	59000 ±22000	44.01	52	20 - 34	1700 - 2900
SO_2	20000 ±7700	64.06	26	9.9 - 17	860 - 1400
H_2S	1200 ±580	34.08	0.82	0.32 - 0.53	27 - 46
HCl	2270 ±1000	36.46	1.7	0.64 - 1.1	55 - 93
HF	510 ±340	20.01	0.20	0.079 - 0.13	6.8 - 11
H_2	2900 ±2900	2.02	0.12	0.045 - 0.076	3.9 - 6.6
			Total:	160 - 270	14000 - 23000

Table 1 Volatile species and their estimated fluxes

6. Discussion

We observed a small vent in the base of a volcanic crater vigorously jetting gas with audible sound akin to jet noise. The temperature contrast between the gasses and ambient atmosphere made the jet easily distinguishable in the thermal IR band, which enabled an estimate of the diameter. The high temperature ratio of the jet is of note as this indicates LST noise will be the dominant noise source over wider range of observation angles (Tam et al., 1996). Figure 5 shows correlated signal from 0.5 to 25 Hz and Figure 6c,f shows consistent spectral structure (i.e. the shape of the PSD curve including peaks and troughs) across array elements in the same frequency band and higher. This is evidence that the acoustic signal from the fumarolic jet is broadband and present in the infrasonic (<20 Hz) to audible range (>20 Hz). The character of the acoustic data is sustained, low-amplitude and broadband. Given these observations, we infer the

sounds observed with microphones and by those in the field at Aso to be jet noise. Assuming it is jet noise, a reasonable jet velocity was estimated (79 – 132 m/s) based on the assumed St = 0.19.

6.1. Wind Noise

Wind can hinder infrasonic detection of low amplitude sources. The lack of correlation between array elements during the initial west crater deployment was likely the result of wind noise overpowering the volcanic signal, as the deployment overlapped with the rainy season in Japan. Figure 5g shows the 10-minute running average wind speed near the summit of Aso from 3 to 11 August 2015. Each time the wind speed increases the MCCM values drop, indicating that the wind masks the jet noise. To reduce wind noise instruments are often deployed in vegetation as this increases surface roughness and reduces wind (Walker and Hedlin, 2009). Other methods for wind noise reduction include arrays of hoses or pipes attached to a sensor or dense arrays of instruments. None of these options were feasible at Aso as there is no vegetation near the summit, as is often the case with active volcanic environments, and space and installation time were limiting factors. Array processing can help reduce wind noise and identify correlated signal. While the wind noise did not correlate between the array elements, there were still times in which it over powered the signal of interest. Wind not only buries signal in noise, but it can also delay or advance the arrival of sound waves particularly when sensors are deployed as a network. These differences in infrasonic arrival time have been used to invert for the wind speed and direction (Marcillo and Johnson, 2010) and shown to affect source location (McKee et al., 2014). We did not observe altered arrival times at Aso given the microphones were deployed in an array in which sound delay should be minimal. Ultimately, wind noise challenges observance of low amplitude signals and should be accounted for in experiment design.

6.2. Jet Noise Spectra

Assuming this fumarolic gas jet behaves similarly to a laboratory jet, certain characteristics are expected in the acoustic spectra. The fumarolic jet has a Mach number of about 0.3 to 0.4 and a high temperature ratio, which suggests the sound is jet-mixing noise and given the small θ, LST is likely the dominant source. Sound from a heated, low Mach jet is not well studied; however, there is a general understanding of the sound mechanisms (Viswanathan, 2004). In supersonic, high Mach number jets, the mechanism for LST sound production is the LST moving and propagating downstream at supersonic speeds. For subsonic jets, the sound is produced by the growth and decay of LST at supersonic speeds. In other words, for supersonic jets the LST has supersonic velocity, while for subsonic jets the LST structures may move downstream at supersonic velocities. LST produces sound primarily at small θ for both subsonic and supersonic jets (Viswanathan, 2009). In turn, spectra dominated by LST are expected at small θ for all jet velocities. The characteristics of jet noise spectra change with respect to θ, D_j, T_j/T_a, and M (Viswanathan, 2004; Viswanathan, 2006; Viswanathan, 2009). While study of hot, low Mach number jets are limited, some trends have been observed. For example as T_j/T_a increases with a small θ, holding all else constant, the sound pressure level decreases at high frequencies, increases at low frequencies, and the spectral peak moves to lower frequencies. If T_j/T_a, D_j, and small θ are held constant and the Mach number decreases, the spectral peak narrows and shifts to lower frequencies (Viswanathan, 2009). The spectral content for Aso's fumarolic jet noise observed at $\theta = 57.6°$ are expected to show a narrowed broadband peak where the low frequencies have higher power than the high frequencies. In other words the spectral shape will

not be a mirror image about the peak. This is not observed in the spectra (Figure 6c,f), which suggests the spectral complexity is related to source or path effects, such as reverberations in the crater, or is related to noisy data. As the data are highly correlated for the time periods in which we scrutinize the spectra, it is more likely the spectra are influenced by source or path.

6.3. Topography

The propagation path was analyzed to address the spectral structure and differences observed in the data between the array elements. The topographic profiles do not show significant differences between the elements, suggesting along-path variations are not the source of spectral differences (Fig. 7). Figure 9c and d show the smoothed spectra from Figure 6f and the power spectral difference between array elements relative to element 1, respectively. In the fumarolic jet spectra there are differences in power between the array elements on the order of 15 dB and distinct peaks (Figs. 6c,f and 9c,d). For jet noise we would expect little to no power difference and a single broad peak that smoothly decays. The SWs (Fig. 8) and their spectra (Fig. 9a) show differences in power, particularly between array elements 1 and 5, but at about an order of magnitude less than the data. While the SWs spectra do not account for all the features in the spectra, there are some similar trends between the two that highlight the influence of the local topography. For example, from 0.1 to about 1 Hz the spectral shape and power in the SWs and data are similar across array elements for the synthetic and observed data, respectively. This is likely because the wavelengths are much longer than the length scale of the topographic features and as such the infrasonic waves are not heavily influenced. At frequencies higher than 1 Hz there are more peaks and increased differences in power. The structures in the spectra are consistent across array elements, particularly in the 2 – 10 Hz range of the data. While this could be a source characteristic, it seems unlikely, as LST jet noise spectra are smooth and we have strong evidence for gas jetting. For that frequency band the wavelengths are 34 (10 Hz) to 170 m (2 Hz) at a sound speed of 340 m/s, which is the same length scale as the crater wall. These consistent structures in the spectra are likely due to waves interacting with the crater wall. Another common trend between the SWs and the data is that at higher frequencies (2-10 Hz) the array elements 2 – 5 have higher power than element 1, with element 5 having the highest power. This could be due to sound reflecting off the partially collapsed pyroclastic cone and thus amplifying the signal at those frequencies. The vent geometry at Tungurahua Volcano, Ecuador has been shown to amplify the acoustic signal such that it propagates as an effective dipole (Kim et al., 2012). Figure 7 suggests the pyroclastic cone located to the west-northwest of the fumarolic jet is significantly affecting sound propagation. The SPL loss is the lowest to the south and east of the jet and there is a sharp contrast in SPL along the partially collapsed pyroclastic cone wall (10s of meter high) by about 20 dB. This suggests the sound is being reflected and amplified to the southeast, which could explain the higher power for the more easterly array elements. The structure in the spectra may be due to the sound interacting with the crater walls and the differences in power related to near vent geometry.

While the SWs and the data have some similar trends in spectral content, they do not match. The SWs are incomplete with respect to the data, which may be due to limitations in the source waveform. However, the source at Aso is likely jet noise, which is broadband and sustained. While the SWs give an initial approximation of the sound radiation and interaction with topography, they do not fully capture the interaction of a sustained, broadband source with the local topography. Future numerical modeling will incorporate more sustained source waveforms

functions. Errors or unresolved topography in the DEM may also contribute to the spectral complexity.

6.4. Volcanic Jet Noise

Our purpose in analyzing fumarolic jet noise is to compare it to volcanic jet noise. Unfortunately, direct comparison of the spectra, is not particularly useful here as the spectra for Aso are highly complex and likely influenced by the local crater topography. However, a qualitative comparison of spectral content is valuable as well as the comparison of waveform characteristics, Strouhal numbers, and observation angles. Table 2 shows the acoustic features determined and observed at several volcanoes where volcanic jet noise has been recorded and for a simulated strong plume (SP) (Cerminara et al., 2016). This table highlights the variability in volcanic jets and their characteristics, as well as the limited infrasonic observations and the challenge in determining jet parameters as only four of the cases prior to this study have all the fields estimated. For the nine cases listed, all are described as sustained, broadband infrasonic signals, but each has a different peak frequency listed under, f [Hz]. Aso's frequency range falls towards the high end, but this is expected, as the jet diameter is likely one to two orders of magnitude smaller than the other examples.

Volcano	St	D_j [m]	v_j [m/s]	D_j/v_j [s]	M	θ [deg.]	f [Hz]	r [km]	Phase	Eruptive style
Kasatochi*[a]	0.4	~750	-	~5 - 10	-	-	0.04 - 0.075	2103	Ash, gas	Plinian
Okmok**[a]	-	-	-	-	-	-	-	1706	Ash, gas	Plinian
Nabro[b]	-	-	>~330	-	>1	~1 - 45	<8	264	Ash poor, gas-rich	Vulcanian to subplinian
Karymsky[c]	-	~150	-	-	-	~92 - 108	15 - 25	2.3 - 4.1	Gas	Gas jetting
Tungurahua[d]	0.4	300 - 400	~300	~1 - 1.33	~0.9	~94 - 98	0.4	36.9	Gas, tephra, ballistics	Vulcanian, subplinian, plinian
MSH[d]	0.06	~30	~100	~0.3	~0.3	>90	0.2	13.4	Gas, tephra	Phreatic explosion
Aso***	0.19	2.5	79 - 132	0.02 - 0.03	0.3 – 0.4	57.6	6 - 10	0.22	Gas	Fumarolic gas jetting
Stromboli[e]	1.2 - 1.8	~2	335 - 432	0.0046 - 0.0060	0.98 – 1.26	60	254 - 305	0.34	Gas, bombs to ash	Strombolian to Vulcanian explosions; gas jetting
Simulated SP[f]	0.32	1406	275	5	1.8	90	~0.07	15		Plinian scenario

Table 2 Comparisons of Volcanic Jet Noise Characteristics

*Fee et al. (2010b) chose St as the eruption was considered to be similar to Tungurahua.

**Fee et al. (2010b) could not definitively say whether the recorded infrasound from Okmok was jet noise due to low the S/N.

***The St for Aso was chosen by the authors and not determined by independent means.

Sources: [a](Fee et al., 2010b), [b](Fee et al., 2013), [c](Rowell et al., 2014), [d](Matoza et al., 2009), [e](Taddeucci et al., 2014), [f](Cerminara et al., 2016)

We now focus on the comparison between Aso and Tungurahua, Mount St. Helens (MSH), Stromboli, and the simulated strong plume from Cerminara et al. (2016), as these examples have all the fields in Table 2 and the recordings are made at relatively close ranges, unlike Kasatochi, Okmok and Nabro where the observations were made at hundreds to thousands of kilometers away. Aso's angle of observation is the smallest achieved so far in volcanic jet noise studies. The Strouhal number assumed for Aso is also much higher than that of MSH and much lower than Tungurahua's, Stromboli's and the simulated case. Aso has a comparable Mach number to

MSH, but much lower than Tungurahua, Stromboli and Simulated SP. While the Mach numbers for Aso and MSH are similar, the Strouhal number shows the difference in length scale between the two. Aso and Stromboli have similar diameters, but vastly different velocities, St and M values. Tungurahua and Simulated SP have much higher Strouhal and Mach numbers, as expected given the significantly larger scale of those eruptions compared to the gas jet at Aso. There are still significant variations between observed and determined jet parameters despite using high-resolution DEMs, numerical modeling, and incorporating visual and IR images. Ultimately, more field observations, simulations, and laboratory experiments are needed to improve our understanding of volcanic jet noise and parameters.

6.5. Jet Noise Parameters and Volatile Mass Flux

The Strouhal number for fumaroles is not known. However, the value for pure-air laboratory jet experiments was found to approach 0.19 when the jet velocity decreased towards ambient speed of sound independent of jet temperature (Tam et al., 1996). Since fumaroles are gas-only and contain no particles, we assume St=0.19 based on the laboratory experiments (Tam et al., 1996). Assuming a Strouhal number of 0.19 results in an estimated velocity of ~79 – 132 m/s for the peak frequency range 6 – 10 Hz, which seems realistic. We note that St numbers of 0.06 (MSH) and 0.4 (Tungurahua) produce less realistic predictions of velocity, particularly for St=0.06 as this estimated supersonic velocities. If the jet velocity were supersonic, we might expect supersonic spectral features such as crackle, which were not observed. By varying the Strouhal number from 0.1 to 0.3 for a peak frequency of 7 Hz, the estimated jet velocity ranges from ~58 – 175 m/s. These estimated velocities are reasonable and highlight the variability in estimated velocity relative to the assumed Strouhal number. In future work, constraining the St for fumaroles (using for example controlled laboratory experiments) would allow us to make more accurate estimates of velocity.

Gas flux is now estimated using the jet velocity and diameter derived from infrasound and thermal data. Table 1 shows our flux estimations for the volatile concentrations available from Shinohara et al. (2015). For comparison and validation purposes we focus on H_2O, SO_2 and the total as these are more commonly discussed and validated. Our acoustically-derived SO_2 flux of ~850 to 1400 tonnes/day is high compared to that found by Shinohara et al. (2015) (200-400 t/d SO_2). However, this high SO_2 flux may be reasonable as the activity at Aso was higher in 2014-2015 than during the Shinohara et al. (2015) study period (2003-2009). From 2003 – 2005, Naka-dake crater lake level dropped and then dried up, followed by some minor ash emissions. From 2006 – 2009, the water returned to its prior level. The fumaroles along the southeastern crater wall are described as high temperature, but not as vigorous or jetting. JMA measured SO_2 flux at Aso on 6 August 2015 at an average of 1100 t/d (with 1600 t/d maximum and 800 t/d minimum detected). As seen in Figure 3a, b, and c, the southeastern wall of the crater has degassing fumaroles. Recent work has shown the SSE wall fumaroles, active during this study, contribute ~12.5% to the total SO_2 flux for the crater (Mori, 2012). Thus we remove their contribution to the total SO_2 flux for comparison (962.5 t/d avg., 1400 t/d max. and 700 t/d min. SO_2 flux). Aso's activity in the year prior to this study included regular strombolian and phreatic explosions. On 14 September 2015, about a month after the infrasound campaign, there was a large phreato-magmatic eruption with an ash plume reaching ~2 km above the crater and pyroclastic flows. Gorely Volcano, Kamchatka is similar to Aso in that they are both calderas with chains of active cones at the center, similar recent explosive activity, regular presence of

acidic crater lakes and vigorous fumarolic activity from a relatively large (meter-sized) fumarole. Our estimated volatile fluxes are similar in magnitude to those recently reported for Gorely Volcano (Aiuppa et al., 2012). Error in our flux estimates could be due to the estimated velocity being too high, poorly picked peak frequencies due to the complex spectra, and low jet temperature due to a high emissivity value. The volatile concentrations in Shinohara et al. (2015) are determined from sampling the plume sourced from several fumaroles. In turn, the concentrations may inflate our flux estimates for just one fumarole.

6.6. Fumaroles and Future Volcanic Jet Noise Research

The motivation for this project and investigating fumarolic jet noise was to see if fumaroles could be used as proxy for larger volcanic jets as they more closely mimic the complex, high temperature, volcanic jet than a laboratory jet does. The jet noise at Aso was low amplitude in the infrasound band with energy concentrated at higher frequencies. Higher frequencies (shorter wavelengths) are more influenced by local topography. In turn, path effects are present in the recorded data and their spectra making comparisons between fumarolic and laboratory high frequency jet noise difficult. At Aso the topography afforded a smaller observation angle, but added complexity to the spectra. Perhaps this is the trade-off between noise and observation angle until we can better account for a sustained, broadband, higher frequency source interacting with local topography. Although they occur less frequently, larger jets with longer wavelengths observed at higher angles may be simpler to investigate for future studies. Another suggested natural test jet are geysers (Demonte and Johnson, 2013). Geysers have been recorded with microphone arrays in Yellowstone National Park, but the multiphase fluid jetting geysers observed were found to be inefficient at perturbing the atmosphere, particularly in the infrasonic band (Johnson et al., 2013). In the same study, some more energetic jetting geysers were observed for a short duration and found to have lower power in the infrasonic band and higher in the acoustic. This suggests geysers may be good analog volcanic jets, but may have similar challenges with topographic features complicating the acoustic wavefield.

7. Conclusions

We have characterized a fumarolic jet at Aso Volcano, Japan using infrasonic and TIR observations. The jet noise produced by a gas jetting fumarole in Naka-dake crater is low amplitude, sustained, and broadband (0.5 to 25+ Hz). These acoustic observations were made at an unusually small angle to the jet axis (57.6 degrees) at relatively close range (~220 m). The spectra were complex with significant structure and power differences likely due to the large, complex crater and near vent topography. Numerical waveforms were computed to investigate this complexity; however frequency limitations and a simple source time function did not fully account for the propagation and reverberation of a sustained, broadband source within a crater. Even given the complex spectra, we derived a reasonable jet velocity (79 – 132 m/s) using TIR images and acoustic data. For future work, it will be important to have an additional data source such as TIR video or high-speed imaging as used by Taddeucci et al. (2014) to estimate jet velocity in order to independently determine the Strouhal number as it is valuable for comparison. Using these values we estimated the total volatile flux at ~14,000 to 23,000 tonnes/day with ~850 to 1,400 tonnes/day in SO_2. While these fluxes are high compared to previous measurements at Aso, the current activity was also higher and our estimates are similar to similar volcanoes worldwide. This marks the first volatile flux estimates using recorded volcanic jet noise with an assumed St and TIR data. Future studies can incorporate more detailed

estimates of jet properties, such as composition and velocity, by simultaneously deploying infrasonic microphones across a greater angular range, TIR high-speed video and UV camera. The combination of these data would enable independent estimates of jet velocity with the TIR video and SO_2 flux with the UV camera, which could be combined with infrasound data to estimate St directly.

8. Acknowledgements

The authors extend a special thank you to Yu-Chih Huang, Shin Yoshikawa, Mitsuru Utsugi, Takuto Minami, and Takahiro Ohkura, and the AVL for their assistance with fieldwork. Thank you to T. Kazama and T. Ohkura for sharing the March 2015 and the May 2015 1m-resolution DEMs of Nakadake crater, respectively. The 2012 1m and 5m resolution DEMs were provided by the Geospatial Information Authority of Japan. Thank you to Guy Tytgat for teaching the K.M. to solder and in help preparing the equipment. Thank you to Taryn Lopez for discussing volatile flux with K.M. This work was supported by the Japan Society for the Promotion of Science and the National Science Foundation, specifically NSF grants EAPSI-1515624 and NSF-EAR-1113294. Helpful reviews from Wes Thelen and an anonymous reviewer greatly improved the manuscript.

9. References

Aiuppa, A., Giudice, G., Liuzzo, M., Tamburello, G., Allard, P., Calabrese, S., Chaplygin, I., McGonigle, A.J.S. and Taran, Y., 2012. First volatile inventory for Gorely volcano, Kamchatka. Geophys. Res. Lett., 39(6): 1-5. doi: 10.1029/2012gl051177

Allaby, A. and Allaby, M., 2003. A Dictionary of Earth Sciences. In: A. Allaby and M. Allaby (Editors), Oxford Paperback Reference. Oxford University Press, Oxford.

Cerminara, M., Esposti Ongaro, T. and Neri, A., 2016. Large Eddy Simulation of gas-particle kinematic decoupling and turbulent entrainment in volcanic plumes. Journal of Volcanology and Geothermal Research: 1-29. doi: 10.1016/j.jvolgeores.2016.06.018

De Angelis, S., Lamb, O.D., Lamur, A., Hornby, A.J., von Aulock, F.W., Chigna, G., Lavallée, Y. and Rietbrock, A., 2016. Characterization of moderate ash-and-gas explosions at Santiaguito volcano, Guatemala, from infrasound waveform inversion and thermal infrared measurements. Geophys. Res. Lett.: 1-8. doi: 10.1002/2016GL069098

Demonte, P.J. and Johnson, J.B., 2013. Characterization and quantification of geyser eruptions: insights from infrasound monitoring at Yellowstone National Park IAVCEI Scientific Assembly, pp. 1-1.

Depuru Mohan, N.K., Prakash, K.R. and Panchapakesan, N.R., 2015. Mixing Augmentation by Multiple Lobed Jets. American Journal of Fluid Dynamics, 5(2): 55-64. doi: 10.5923/j.ajfd.20150502.03

Fee, D., Garces, M. and Steffke, A., 2010a. Infrasound from Tungurahua Volcano 2006–2008: Strombolian to Plinian eruptive activity. Journal of Volcanology and Geothermal Research, 193(1-2): 67-81. doi: 10.1016/j.jvolgeores.2010.03.006

Fee, D., Haney, M.M., Matoza, R.S., Van Eaton, A.R., Cervelli, P., Schneider, D.J. and Iezzi, A.M., 2017. Volcanic tremor and plume height hysteresis from Pavlof Volcano, Alaska. Science, 355(6320): 45-48. 10.1126/science.aah6108

Fee, D. and Matoza, R.S., 2013. An overview of volcano infrasound: From hawaiian to plinian, local to global. Journal of Volcanology and Geothermal Research, 249: 123-139. doi: 10.1016/j.jvolgeores.2012.09.002

Fee, D., Matoza, R.S., Gee, K.L., Neilsen, T.B. and Ogden, D.E., 2013. Infrasonic crackle and supersonic jet noise from the eruption of Nabro Volcano, Eritrea. Geophysical Research Letters, 40(16): 4199-4203. doi: 10.1002/grl.50827

779 Fee, D., Steffke, A. and Garces, M., 2010b. Characterization of the 2008 Kasatochi and Okmok eruptions
780 using remote infrasound arrays. Journal of Geophysical Research, 115. doi:
781 10.1029/2009jd013621
782 Fee, D., Yokoo, A. and Johnson, J.B., 2014. Introduction to an open community infrasound dataset from
783 the actively erupting Sakurajima Volcano, Japan. Seismological Research Letters. doi:
784 10.1785/0220140051
785 Fischer, T.P., 2008. Fluxes of volatiles (H2O, CO2, N2, Cl, F) from arc volcanoes. Geochem. J., 42(1):
786 21-38. doi: 10.2343/geochemj.42.21
787 Goto, A., Ripepe, M. and Lacanna, G., 2014. Wideband acoustic records of explosive volcanic eruptions
788 at Stromboli: New insights on the explosive process and the acoustic source. Geophys. Res. Lett.,
789 41(11): 3851-3857. doi: 10.1002/2014GL060143
790 Johnson, J.B., Anderson, J.F., Anthony, R.E. and Sciotto, M., 2013. Detecting geyser activity with
791 infrasound. Journal of Volcanology and Geothermal Research, 256: 105-117. doi:
792 10.1016/j.jvolgeores.2013.02.016
793 Johnson, J.B. and Ripepe, M., 2011. Volcano infrasound: A review. Journal of Volcanology and
794 Geothermal Research, 206(3-4): 61-69. doi: 10.1016/j.jvolgeores.2011.06.006
795 Kaneko, K., Kamata, H., Koyaguchi, T., Yoshikawa, M. and Furukawa, K., 2007. Repeated large-scale
796 eruptions from a single compositionally stratified magma chamber: An example from Aso
797 volcano, Southwest Japan. Journal of Volcanology and Geothermal Research, 167. doi:
798 10.1016/j.jvolgeores.2007.05.002
799 Kaneshima, S., Kawakatsu, H., Matsubayashi, H., Sudo, Y., Tsutsui, T., Ohminato, T., Ito, H., Uhira, K.,
800 Yamasato, H., Oikawa, J., Takeo, M. and Iidaka, T., 1996. Mechanism of Phreatic Eruptions at
801 Aso Volcano Inferred from Near-field Broadband Seismic Observations. Science, 273: 642-645.
802 doi: 10.1126/science.273.5275.642
803 Kim, K., Fee, D., Yokoo, A. and Lees, J.M., 2015. Acoustic source inversion to estimate volume flux
804 from volcanic explosions. Geophysical Research Letters, 42(13): 5243-5249. doi:
805 10.1002/2015GL064466
806 Kim, K. and Lees, J., 2014. Local Volcano Infrasound and Source Localization Investigated by 3D
807 Simulation. Seismological Research Letters. doi: 10.1785/0220140029
808 Kim, K. and Lees, J.M., 2011. Finite-difference time-domain modeling of transient infrasonic wavefields
809 excited by volcanic explosions. Geophysical Research Letters, 38(L06804). doi:
810 10.1029/2010gl046615
811 Kim, K., Lees, J.M. and Ruiz, M., 2012. Acoustic multipole source model for volcanic explosions and
812 inversion for source parameters. Geophysical Journal International, 191: 1192-1204. doi:
813 10.1111/j.1365-246X.2012.05696.x
814 Kundu, P.K. and Cohen, I.M., 2008. Fluid Mechanics. Academic Press.
815 Lacanna, G. and Ripepe, M., 2013. Influence of near-source volcano topography on the acoustic
816 wavefield and implication for source modeling. Journal of Volcanology and Geothermal
817 Research, 250: 9-18. doi: 10.1016/j.jvolgeores.2012.10.005
818 Lee, D.-C., Olson, J.V. and Szuberla, C.A.L., 2013. Computationally robust and noise resistant numerical
819 detector for the detection of atmospheric infrasound. J. Acoust. Soc. Am., 134(1): 862-868. doi:
820 10.1121/1.4807802
821 Lighthill, M.J., 1952. On sound generated aerodynamically. I. General theory. Proceedings of the Royal
822 Society of London A: Mathematical, Physical and Engineering Sciences, 211(1107): 564-587.
823 doi: 10.1098/rspa.1952.0060
824 Lillesand, T.M., Kiefer, R.W. and Chipman, J.W., 2008. Remote Sensing and Image Interpretation. John
825 Wiley & Sons, Inc., USA, 756 pp.
826 Lopez, T.M., Fee, D., Prata, F. and Dehn, J., 2013. Characterization and interpretation of volcanic activity
827 at Karymsky Volcano, Kamchatka, Russia, using observations of infrasound, volcanic emissions,
828 and thermal imagery. Geochem. Geophys. Geosyst., 14(12): 5106-5127. doi:
829 10.1002/2013GC004817

Lopez, T.M., Tassi, F., Aiuppa, A., Galle, B., Rizzo, A., Fiebig, J., Capecchiacci, F., Giudice, G., Caliro, S., Ketner, D., Tamburello, G. and Paskievitch, J.F., in prep. Geochemical constraints on volatile sources and subsurface conditions at Mount Martin, Mount Mageik, and Trident Volcanoes, Katmai Volcanic Cluster, Alaska. Journal of Volcanology and Geothermal Research.

Marcillo, O. and Johnson, J.B., 2010. Tracking near-surface atmospheric conditions using an infrasound network. The Journal of the Acoustical Society of America, 128(1): 14 - 19. doi: 10.1121/1.3442725

Matoza, R.S., Fee, D. and Garces, M.A., 2010. Infrasonic tremor wavefield of the Pu'u 'O'o crater complex and lava tube system, Hawaii, in April 2007. J Geophys Res-Sol Ea, 115. doi: 10.1029/2009jb007192

Matoza, R.S., Fee, D., Garcés, M.A., Seiner, J.M., Ramón, P.A. and Hedlin, M.A.H., 2009. Infrasonic jet noise from volcanic eruptions. Geophysical Research Letters, 36(8). doi: 10.1029/2008gl036486

Matoza, R.S., Fee, D., Neilsen, T.B., Gee, K.L. and Ogden, D.E., 2013. Aeroacoustics of volcanic jets: Acoustic power estimation and jet velocity dependence. Journal of Geophysical Research, 118: 6269–6284. doi: 10.1002/2013JB010303

McKee, K., Fee, D., Rowell, C. and Yokoo, A., 2014. Network-Based Evaluation of the Infrasonic Source Location at Sakurajima Volcano, Japan. Seismological Research Letters, 85(6): 1200-1211. doi: 10.1785/0220140119

Mori, T., 2012. Measurement of SO2 flux ratio between two plumes of the 1st crater of Nakadake, Aso volcano, Japan. Chikyu, 34: 732-737.

Prieto, G.A., Parker, R.L., Thomson, D.J., Vernon, F.L. and Graham, R.L., 2007. Reducing the bias of multitaper spectrum estimates. Geophysical Journal International, 171(3): 1269-1281. doi: 10.1111/j.1365-246X.2007.03592.x

Pritchard, P.J., 2011. Dimensional Analysis and Similitude, Fox and McDonald's Introduction to Fluid Mechanics. John Wiley & Sons, Inc., Hoboken, NJ, pp. 290 - 327.

Rowell, C., Fee, D., Szuberla, C.A., Arnoult, K.M., Matoza, R.S., Firstov, P.P., Kim, K. and Makhumdov, E., 2014. Three-dimensional volcano-acoustic source localization at Karymsky Volcano, Kamchatka, Russia. Journal of Volcanology and Geothermal Research, 283: 101-115. doi: 10.1016/j.jvolgeores.2014.06.015

Shinohara, H., Yoshikawa, S. and Miyabuchi, Y., 2015. Degassing Activity of a Volcanic Crater Lake: Volcanic Plume Measurements at the Yudamari Crater Lake, Aso Volcano, Japan, Volcanic Lakes. Springer Berlin Heidelberg, pp. 201-217.

Taddeucci, J., Sesterhenn, J., Scarlato, P., Stampka, K., Del Bello, E., Fernandez, J.J.P. and Gaudin, D., 2014. High-speed imaging, acoustic features, and aeroacoustic computations of jet noise from Strombolian (and Vulcanian) explosions. Geophysical Research Letters, 41(9): 3096-3102. doi: 10.1002/2014GL059925

Takagi, N., Kaneshima, S., Kawakatsu, H., Yamamoto, M., Sudo, Y., Ohkura, T., Yoshikawa, S. and Mori, T., 2006. Apparent migration of tremor source synchronized with the change in the tremor amplitude observed at Aso volcano, Japan. Journal of Volcanology and Geothermal Research, 154(3-4): 181-200. 10.1016/j.jvolgeores.2006.02.001

Tam, C.K.W., 1995. Supersonic Jet Noise. Annu Rev Fluid Mech, 27: 17-43. doi: 10.1146/Annurev.Fl.27.010195.000313

Tam, C.K.W., 1998. Jet Noise: Since 1952. Theoretical and Computational Fluid Dynamics, 10: 393-405. doi: 10.1007/s001620050072

Tam, C.K.W. and Burton, D.E., 1984. Sound Generated by Instability Waves of Supersonic Flows .2. Axisymmetric Jets. J Fluid Mech, 138(Jan): 273-295. doi: 10.1017/S0022112084000124

Tam, C.K.W. and Chen, P., 1994. Turbulent Mixing Noise from Supersonic Jets. Aiaa J, 32(9): 1774-1780. doi: 10.2514/3.12173

Tam, C.K.W., Golebiowski, M. and Seiner, J.M., 1996. On the Two Components of Turbulent Mixing Noise from Supersonic Jets. Aiaa J: 1-19. doi: 10.2514/6.1996-1716

Tam, C.K.W., Viswanathan, K., Ahuja, K.K. and Panda, J., 2008. The sources of jet noise: experimental evidence. J Fluid Mech, 615: 253-292. doi: 10.1017/S0022112008003704

Thelen, W.A. and Cooper, J., 2015. An analysis of three new infrasound arrays around Kīlauea Volcano. 2014-1253. doi: 10.3133/ofr20141253

Thomson, D.J., 1982. Spectrum Estimation and Harmonic Analysis. Proceedings of the IEEE, 70(9): 1055-1096. doi: 10.1109/PROC.1982.12433

Viswanathan, K., 2004. Aeroacoustics of hot jets. J Fluid Mech, 516: 39-82. doi: 10.1017/S0022112004000151

Viswanathan, K., 2006. Scaling laws and a method for identifying components of jet noise. Aiaa J, 44(10): 2274-2285. doi: 10.2514/1.18486

Viswanathan, K., 2009. Mechanisms of jet noise generation: classical theories and recent developments. Int J Aeroacoust, 8(4): 355-407. doi: 10.1260/147547209787548949

Walker, K.T. and Hedlin, M.A.H., 2009. A Review of Wind-Noise Reduction Methodologies. In: A. Le Pichon, E. Blanc and A. Hauchecorne (Editors), Infrasound Monitoring for Atmospheric Studies. Springer Netherlands, pp. 141-182.

Wallace, P.J., 2005. Volatiles in subduction zone magmas: concentrations and fluxes based on melt inclusion and volcanic gas data. Journal of Volcanology and Geothermal Research, 140(1): 217-240. doi: 10.1016/j.jvolgeores.2004.07.023

Woulff, G. and McGetchin, T.R., 1976. Acoustic Noise from Volcanoes: Theory and Experiment. Geophysical Journal of Research, 45: 601-616. doi: 10.1111/j.1365-246X.1958.tb05346.x

Yokoo, A., Iguchi, M., Tameguri, T. and Yamamoto, K., 2013. Processes Prior to Outbursts of Vulcanian Eruption at Showa Crater of Sakurajima Volcano. Bulletin of the Volcanological Society of Japan, 58(1): 163-181. http://www.kazan-g.sakura.ne.jp/Vol/58p163a.pdf

Yokoo, A. and Miyabuchi, Y., 2015. Eruption at the Nakadake 1st Crater of Aso Volcano Started in November 2014. Bulletin of the Volcanological Society of Japan, 60(2): 275-278. http://ci.nii.ac.jp/naid/110009976000/en/

Yokoo, A. and Taniguchi, H., 2004. Application of video image processing to detect volcanic pressure waves: A case study on archived images of Aso Volcano, Japan. Geophysical Research Letters, 31(23). doi: 10.1029/2004gl021183